REPORT DOCUMENTATION PAGE

Form Approved
OMB No. 0704-0188

1. REPORT DATE (DD-MM-YYYY) 1Jan 2005	2. REPORT TYPE Final Technical Report	3. DATES COVERED (From – To) 1 Jan 2005-30 Jun 2008

4. TITLE AND SUBTITLE Knowledge Oriented Materials Engineering of Layered Thermal Barrier System (Nomelt)	5a. CONTRACT NUMBER
	5b. GRANT NUMBER FA9550-05-1-0173
	5c. PROGRAM ELEMENT NUMBER
6. AUTHOR(S) Kevin J. Hemker, Johns Hopkins University	5d. PROJECT NUMBER
	5e. TASK NUMBER
	5f. WORK UNIT NUMBER

7. PERFORMING ORGANIZATION NAME(S) AND ADDRESS(ES) Johns Hopkins University Baltimore, MD	8. PERFORMING ORGANIZATION REPORT NUMBER

9. SPONSORING/MONITORING AGENCY NAME(S) AND ADDRESS(ES) USAF/AFRL AFOSR 875 North Randolph Street Arlington VA 22203	10. SPONSOR/MONITOR'S ACRONYM(S) AFOSR
	11. SPONSORING/MONITORING AGENCY REPORT NUMBER N/A

12. DISTRIBUTION AVAILABILITY STATEMENT

Distribution Statement A: Approved for public release. Distribution is unlimited.

13. SUPPLEMENTARY NOTES

14. ABSTRACT

The proposed work is of significant importance to the technological needs of the Air Force. The thermal barriers used in gas turbines comprise multi-layers with multiple functions. The extreme environments impose a harsh set of requirements on engine materials and require a new class of barrier coatings. This model based approach to designing new thermal barrier materials will enable the quantitative prediction of performance and exploit the full potential of new materials for these applications.

15. SUBJECT TERMS

16. SECURITY CLASSIFICATION OF:			17. LIMITATION OF ABSTRACT	18. NUMBER OF PAGES 11	19a. NAME OF RESPONSIBLE PERSON		
a. REPORT Unclassified	b. ABSTRACT Unclassified	c. THIS PAGE Unclassified	Unclassified		19b. TELEPONE NUMBER (Include area code) (703)		

Standard Form 298 (Rev. 8-98)
Prescribed by ANSI-Std Z39-18

MEANS II: KNOWLEDGE ORIENTED MATERIALS ENGINEERING OF LAYERED THERMAL BARRIER SYSTEMS (NOMELT)

Kevin J. Hemker, Johns Hopkins University

FINAL REPORT

Reporting Period: January 1, 2005 – June 30, 2008

In collaboration with:

(FA9550-05-1-0203, FA9550-05-1-0229, FA9550-05-1-0039, FA9550-05-1-0163)

Anthony Evans, University of California Santa Barbara

Peggy Hou, Lawrence Berkeley National Laboratory

John Hutchinson, Harvard University

Tresa Pollock, University of Michigan

John Smith, Delphi Research Laboratory

David Srolovitz. Princeton University

Summary

The MEANS-2 NOMELT team developed a design code for one of the prevailing failure modes in thermal barrier systems used for aero-turbines; abrupt delamination along the interface between the thermally grown oxide (TGO) and the intermetallic bond coat. The project involved experimental characterization of the various layers, first principles calculations of the interface, and the addition of strain gradient plasticity to a mechanics code for interfacial delamination. The integration of these efforts provided a pathway for describing TBC delamination in a way that incorporates: atomic-scale first-principles descriptions of interfacial bonding (as a function of chemistry); micro- and nano-scale measurements of plasticity (including strain gradient length scales); elastic behavior of the top and bond coats; and a continuum-level description of the stresses that develop during thermal cycling. This type of integrated length-scale modeling has never been accomplished before for a problem that incorporates atomistics with plasticity and fracture. It predicts trends in the toughness with stoichiometry, segregation and dopant, as a function of the yield strength of the bond coat adjacent to the interface and the characteristic plasticity length scale due to the geometrically-necessary dislocations that accumulate in the plastic zone.

The focus of this report in on the unique experimental characterization developed and conducted at Johns Hopkins University. A brief summary of overall project integration is also included to provide context for the detailed experimental investigations that were undertaken.

Research Objectives

The overarching objective of NOMELT was to develop a design code to characterize TBC delamination, which occurs at the interface of the TGO and a two-phase bond coat in a commercial TBC. The constituent models developed to support this code addressed three specific time/cycle dependent phenomena: (i) evolution of microstructure and properties of the bond coat, (ii) changes in the structure and properties of the ceramic top coat, (iii) the role of chemistry in atomic bonding across the interface. These findings were incorporated into an mechanics-based interfacial delamination model adapted for this problem through the addition of strain gradient plasticity.

In addition to overall management of the integrated research team, activities at Johns Hopkins focused on experimental characterization of the bond coat and top coat and measurement of the interfacial toughness of the bond coat–TGO interface. Transmission electron microscopy and novel micro-mechanical testing were developed and employed, and the results from these experimental activities were passed to the modelers and used to support development of an overarching design code.

Research Activities

NOMELT experimental research activities at Johns Hopkins focused on five specific tasks; (i) microstructural characterization of the bond coat, (ii) mechanical characterization of the bond coat, (iii) measurement a strain gradient length scale parameter for the bond coat, (iv) determination of the in-plane elastic modulus of the 7YSZ top coat, and (v) measurement of the interfacial toughness of the bond coat–TGO interface. Transmission electron microscopy and novel micro-mechanical testing were developed and employed to accomplish these tasks. The experimental methodology and results from these experimental activities are described in the next section. The result of the Hopkins effort was directly integrated into the modeling effort of Evans and Hutchinson and was critical to the development of the overarching design code.

Research Results

I. Microstructural characterization of the bond coat.

The NOMELT program focused on two-phase NiCoCrAlY bond coats with a composition of 40.4 at% Ni, 18.8% Co, 16.4% Cr, 23.3% Al, 0.3% Y, 0.1% Hf and 0.7% Si that were low pressure plasma sprayed (LPPS), shot peened and given a standard densification heat treatment at Pratt and Whitney, USA. Cylindrical and wedge shaped laboratory samples of this bond coat on PWA 1484 were investigated. Studies on bond coat evolution have examined the volume fractions and lattice parameters of the B2 and γ phases in the as-deposited condition and after annealing at 890°C, 950°C, 1000°C, 1050°C, 1100°C and 1150°C. Detailed microprobe studies have focused on the γ layer that forms just below the TGO, as delamination occurs along this interface. Additionally,

characterization of the bond coat, in small pieces of airfoil from blades removed from service at the end of life, has been conducted.

Figure 1 compares the structure of the bond coat in the as-deposited condition with two blade sections which experienced lower temperatures/higher cycles and higher cycles/lower temperatures. With time during service it is apparent that Al is depleted from the bond coat, due to the formation of the Al_2O_3 TGO. As a result, the volume fraction of the B2 NiAl-based phase decreases, particularly within the upper 20 microns of the bond coat, and the Al content of the γ layer just beneath the TGO also decreases. The volume fraction of the B2 phase was measured to decrease as the exposure temperature increased.

As-deposited (Bar J)	Low T / High Cycle Blade	High T / Low Cycle Blade

	$V_f \gamma$ (%)	V_f B2 (%)
Top 10μm	45.5	54.5
Top 20μm	42.3	57.7
Total Thickness	49.2	50.8

	$V_f \gamma$ (%)	V_f B2 (%)
Top 10μm	86.8	13.2
Top 20μm	78.5	21.5
Total Thickness	64.0	36.0

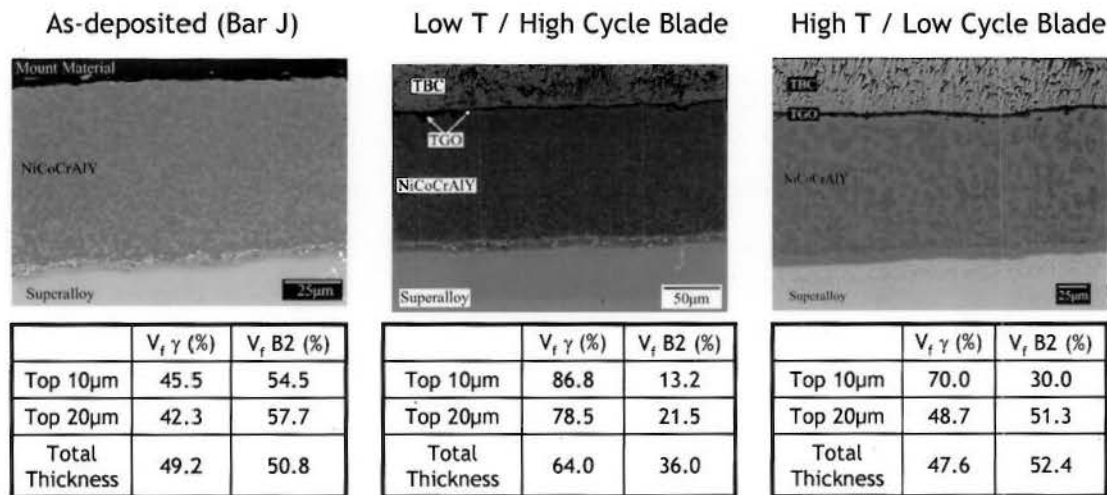|	$V_f \gamma$ (%)	V_f B2 (%)
Top 10μm	70.0	30.0
Top 20μm	48.7	51.3
Total Thickness	47.6	52.4

Fig 1: Comparison of initial coating structure and evolution of phases with cycling in two turbine airfoil samples.

TEM was used to characterize the microstructure of NiCoCrAlY bond coats at different stages of thermal cycling as well as bond coats that had seen service in commercial engine environments. Traditionally, NiCoCrAlY coatings are considered to consist of a NiAl based β-phase and Ni solid solution γ-phase. The latter however, contained fine, coherent precipitates of γ' (Ni_3Al) ~7 nm in size in the as-prepared bond coat and ~24 nm for the thermal cycled specimen (Figs. 2(a) and (b)). The unreasonably slow rates of coarsening suggests that γ' is not a stable, equilibrium phase at the peak thermal cycling temperature of 1100°C but rather forms during cooling. Phase equilibria calculations on the Ni-Co-Cr-Al quaternary support this conclusion.

In single-phase (Ni,Pt)Al bond coats superalloy-bond coat interdiffusion can lead to a martensitic transformation that has a critical effect on the failure mechanism of the TBC system. Fig. 2(d) shows that with thermal cycling the β-phase in the as-prepared NiCoCrAlY bond coat (Fig. 2(c)) also transforms to $L1_0$ martensite. TEM *in-situ* heating of the martensite revealed complete transformation to the β-phase at ~100°-140°C while the reverse transformation took place at ~50°-80°C on cooling. Therefore, although the strain produced by the volumetric change of the transformation is expected to be large the

low transformation temperature together with the fact that NiCoCrAlY coatings are 'two phase' materials strongly indicate that martensite is not significant in this system.
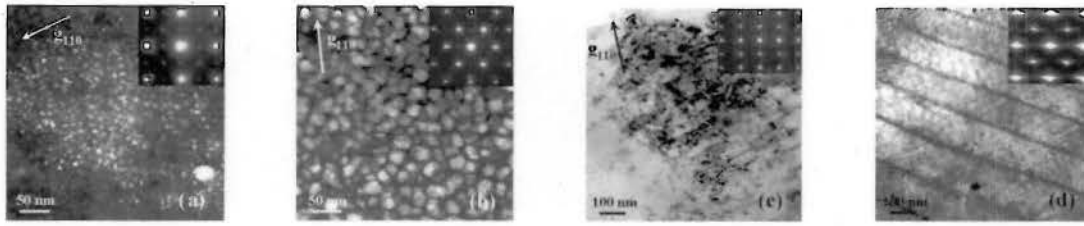

Fig. 2: Dark field images of γ' precipitates in the γ-phase of (a) the as-prepared bond coat and (b) thermal cycled bond coat. β-phase grains in the as-prepared bond coat (c) transform to martensite after thermal cycling (d).

TBC systems based on NiCoCrAlY bond coats typically fail by delamination at the thermally grown oxide (TGO)-bond coat interface. Sulfur impurities greatly reduce adherence and lead to premature oxide spallation. Reactive elements such as Y and Hf in the coating are thought to improve lifetime by forming stable sulfides and / or oxy-sulfides but direct evidence for this has been hard to come by. Using Scanning TEM (STEM) we have detected S precipitates within 'pegs' in a NiCoCrAlY bond coat that had seen service in a commercial engine (Fig. 3). The 'peg' (i.e. regions of abnormal oxide growth) in this case appears to have formed by entrapment of a Y-rich intermetallic by 'folding' of the surface during shot peening. The result highlights the role of reactive elements in gettering the S before it reaches the TGO-bond coat interface and causes embrittlement.
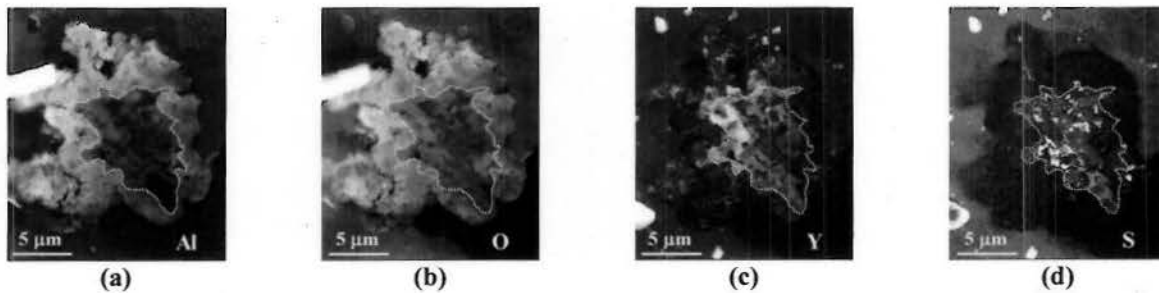

Fig. 3: STEM maps of (a) Al, (b) O, (c) Y and (d) S distribution within an oxide peg.

II. Bond coat mechanical properties.

Micro-tensile testing. The tensile behavior of the bond coat was characterized in two states, as-processed and after 200 thermal cycles. The thermally cycled samples were exposed to a standard furnace cycle test during which they were heated to 1100°C in 10 minutes, held at 1100°C for 45 minutes and then cooled to 100°C within 10 minutes. Micro-tensile specimens were prepared by scalping 700 micron slices from the substrate with a wire-EDM and punching individual microsamples with a specially shaped graphite electrode and a sink-EDM. The substrate, interdiffusion zone and TGO were polished away until the two-phase microstructure of the NiCrAlY bond coat was visible in the optical microscope on both sides.

A custom micro-tensile testing setup was used to measure the mechanical properties of the NiCrAlY bond coat. The setup consists of a piezoelectric motor, load cell, displacement gage, air bearing and a Pixelink digital camera. Strain was measured by digital image correlation. The digital image correlation code was written in Matlab.

The room temperature stress-strain curves for as-processed and thermally cycled bond coats are shown in Fig. 4(a). The as-processed bond coats were found to have a 0.2% yield strength of approximately 1,200 MPa and to support tensile elongations of up to 0.75% plastic strain. For thermally cycled specimens a 0.2% yield strength of 660 MPa and up to 1.5% plastic strain was observed. Although TGO pegs were observed to penetrate into the thermally cycled bond coat, failure was not associated with the presence of these pegs. The elongations to failure reported in Fig. 4 were limited by the sample design; all micro-tesnile samples failed at a stress concentration that developed near the grips.
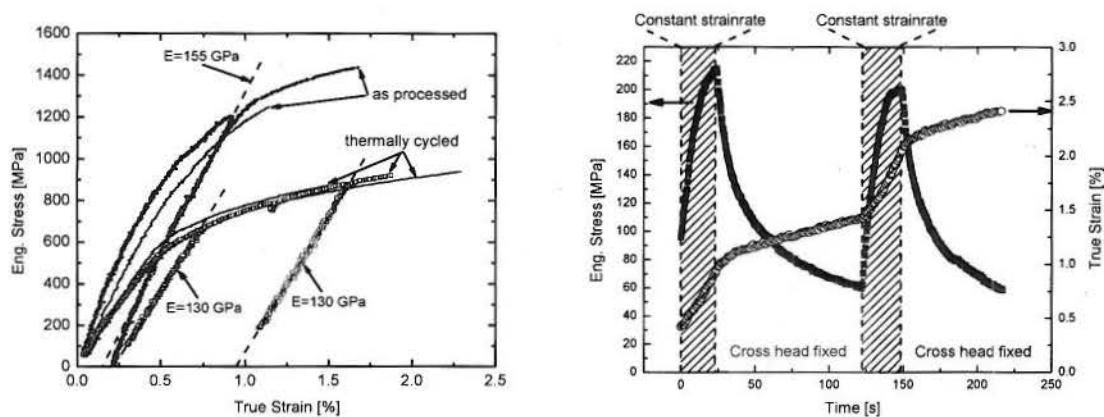

Fig. 4: (a) Stress-strain curves of two as-processed and three thermally cycled NiCoCrAlY bond coat microsamples showing their mechanical behavior at 22°C, and (b) stress and strain versus time of alternating constant strain rate and stress relaxation tests of an as-processed NiCoCrAlY bond coat at 500°C.

It is interesting to note that the ductility exhibited by the NiCoCrAlY bond coats far exceeds what was observed for Pt-modified diffusion aluminide bond coats, which exhibit linear elastic behavior and fail in a brittle manner at all temperatures below its brittle-to-ductile transition temperature (DBTT) of approximately 600°C. Also contrary to what was observed in the diffusion aluminide samples, thermally cycling the NiCoCrAlY bond coat resulted in a reduction in strength and increase in room temperature ductility. In the diffusion aluminide samples formation of the $L1_0$ martensite resulted in stronger bond coats, but that is not the case for the NiCoCrAlY bond coat. The high room temperature strength and ductility exhibited by the NiCoCrAlY bond coat can be expected to retard interfacial crack growth during delamination, which suggests that delamination at the bond coat/TGO interface should actually be easier in the diffusion aluminide bond coat. The fact that delamination is not observed in this system suggest that it is either harder to nucleate the delamination in diffusion aluminide bond coat systems or that that ratcheting is accelerated in these systems as a result of high TGO growth stresses.

Elevated temperature experiments conducted at 500°C are shown in Fig. 4(b). An as-processed bond coats were subjected to a series of repeated constant strain rate experiments,

followed by stress relaxation experiments in which the cross-head was fixed and the stress allowed to relax. Stress and strain are both plotted as a function of time in Fig. 4. The imposed strain rate was on the order of 2×10^{-4} s^{-1} while the strain rate measured during the relaxations was closer to 2×10^{-5} s^{-1} and remarkably constant during the relaxation. The elevated temperature yield strength of the NiCoCrAlY bond coat was measured to be considerably lower than the RT strength and the extent of the relaxation (from 200 MPa to 50 MPa in less than 2 minutes) that occurred when the crosshead was fixed is impressive. Although its RT properties are superior, the intermediate and high temperature strength of the NiCoCrAlY bond coat was found to be lower than that measured for Pt-modified diffusion aluminide bond coats. In this light, it appears that the strength of the NiCoCrAlY bond coat is not what prevents this TBC system from ratcheting.

The electron back scattered SEM image presented in Fig. 5 provides a vivid indication of the coarsening that occurs as a result of thermal cycling. In separate studies, isothermal heat treatment of this bond coat has shown that the volume fraction of phases, their domain size and the chemical composition of each phase evolves as a result of TGO formation and interdiffusion with the underlying substrate. The end result of thermal cycling is a coarser and increasingly Ni-rich bond coat.
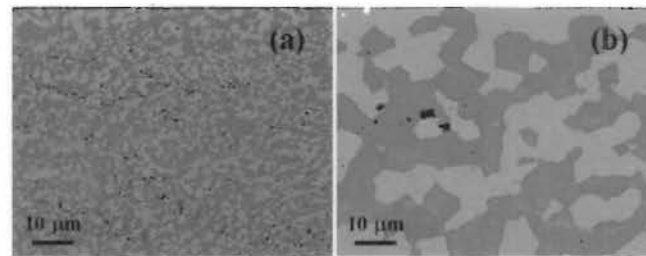

Fig. 5: Backscattered SEM images of (a) as-processed and (b) thermal cycled bond coat. Both images are at the same magnification and direct comparison highlights the coarsening of the microstructure that occurs as a result of thermal cycling.

The presence of ultra-fine γ' precipitates shown in Fig. 2 may be used to explain the remarkable room temperature strength that we have measured for these bond coats. As described in the previous sections, the γ' particles were observed to coarsen slightly as a result of thermal cycling, but the change in mean size, from 7 nm (standard deviation of 3 nm for ~50 precipitates) to 26 nm (standard deviation of 8 nm for ~300 precipitates), is not as great as might have been expected for such extreme thermal treatments. Phase equilibria calculations estimate the γ' solvus temperature for this NiCoCrAlY bond coat to be approximately 750°C and the absence of significant coarsening suggests that the γ' particles are dissolving and re-precipitating out on each thermal cycle. The dissolution of γ' precipitates at higher temperatures might explain why the strength of NiCoCrAlY at elevated temperature is lower than for the Pt-modified diffusion aluminide bond coats. Without precipitation strengthening, the two phase alloy ($\gamma + \gamma'$) would be expected to be weaker at elevated temperatures than single-phase β.

Nanoindentation experiments. The fracture toughness of an interface between a brittle ceramic and a plastically deforming metal is heavily determined by the plastic deformation of

the metal at the crack tip. Strain gradient theory allows one to calculate the behavior of the material in the near vicinity of the crack tip based on experimental measurements of the 'length scale parameters'. The length scale parameters relevant for mode I fracture can be accessed by nanoindentation experiments. Microstructural investigations have shown that the TGO formation depletes the region in the top coat close to the interface from Al, leading to the formation of a γ-Ni layer.

Cross sections of thermally cycled and iso-thermally annealed burner rig bars as well as sections from a turbine blade (in service) were mechanically polished to a mirror finish. The samples were then carefully electro- polished to reduce the roughness and remove any damage caused by the mechanical polishing. Nanoindentation experiments have been carried out at UCSB and through collaborations with Nix at Stanford University. Do to difficulties associated with measuring the properties of extremely small precipitates, bulk samples with the same chemistry and microstructure of the near-TGO γ layer was prepared by Pollock and coworkers at the University of Michigan. These bulk samples were indented through collaboration with Pharr at the University of Tennessee and the experimental results of this study are shown in Fig. 6.
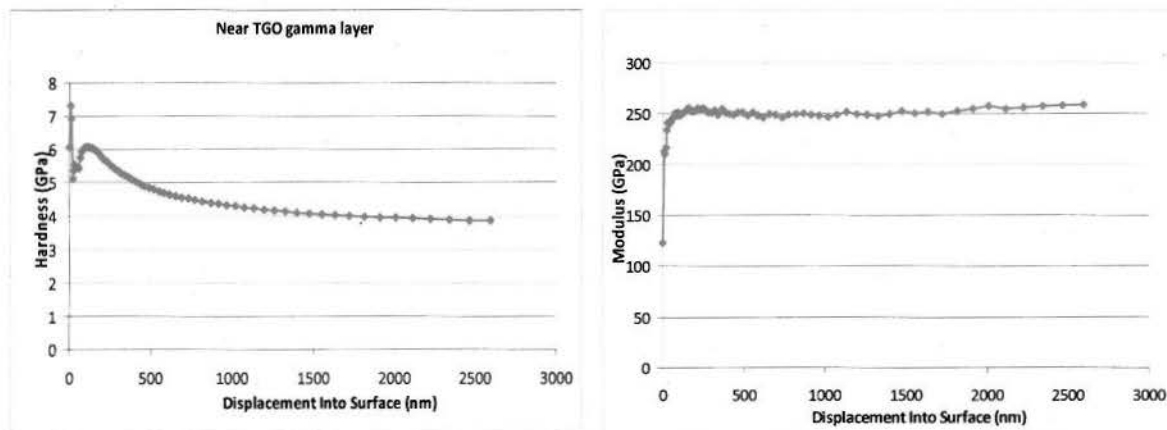

Fig. 6: Experimental measurements of the (a) hardness and (b) elastic modulus of the near-TGO gamma layer as a function of hardness depth. The indentation size effect measured in (a) is used to determine the length scale parameter in Fig. 7.

These measurements of the indentation size effect, e.g. hardness as a function of indentation depth, allow for extraction of a strain gradient length scale parameter (l_1) that is needed in the mechanics-based delamination model. This length scale was extracted through comparison of the experimental data with a normalized plot of the indentation size effect as predicted by strain gradient plasticity, see Fig. 7. The result of this comparison yielded a length scale parameter (l_1) of 50 nm.
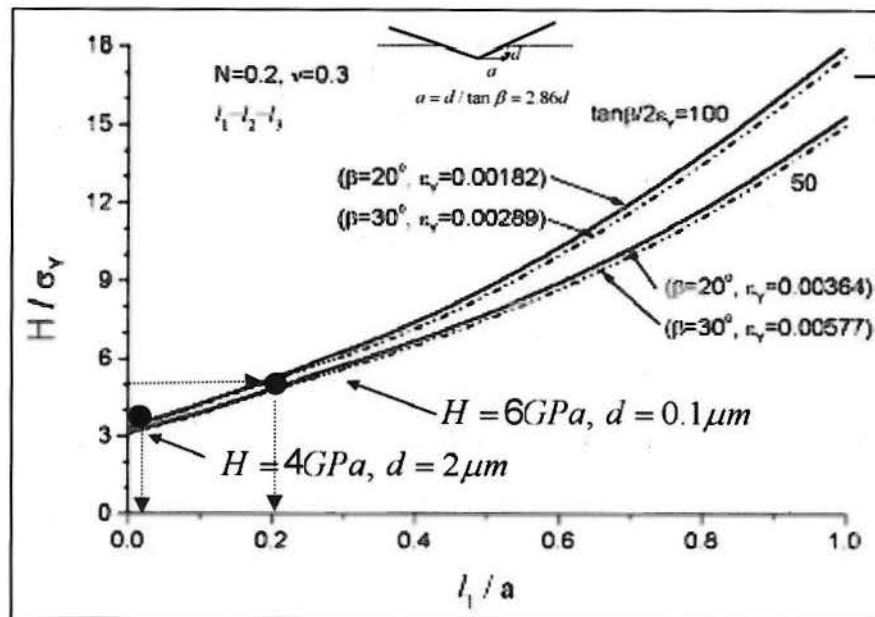
Fig. 7: Determine the length scale parameter from the data in Fig. 6. Consideration of the bond coat tensile properties reported in Fig. 4, the geometry of the indenter, strain gradient plasticity formulations, and the data reported in Fig. 6 yield a length scale parameter (l_1) of 50nm.

CTE measurements. A noncontact high temperature digital image correlation technique has been developed in a parallel NSF supported project and is now being used to evaluate the coefficient of thermal expansion, as a function of temperature, for a number of alloys associated with contemporary thermal barrier coating systems to over $1000°C$. In measurements relevant to the current study, we have measure the temperature dependence of the CTE of the two-phase bond coat, near-TGO gamma layer and underlying superalloy as a function of temperature. The results of these measurements are given in Fig. 8, where it is
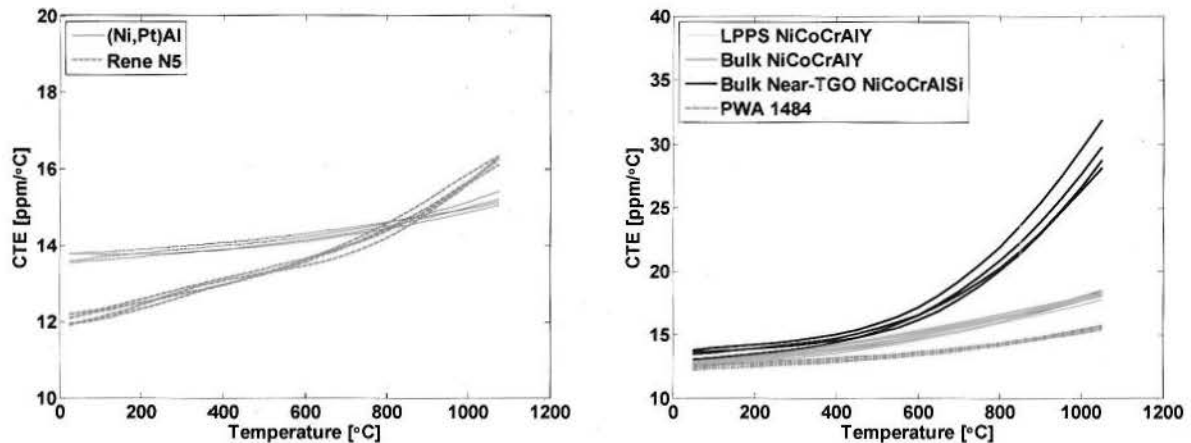

Fig. 8: Measured values of the CTE as a function of temperature for **(a)** a diffusion aluminide system and **(b)** a two-base bond coat system. The data in **(b)** was measured for and used in the current study.

clear that the variation in CTE is fundamentally different than has been measured in single-phase diffusion aluminide bond coat systems. The expansion rate of the bond coats was found to be slightly higher than for the underlying substrate. The extremely high expansion associated with the near-TGO gamma layer is especially intriguing, was not included in the models developed in the current program, but deserves further attention.

IV. A Method for In Situ Measurement of the Strain Dependence of the Elastic Properties of a Columnar Thermal Barrier Coating

TBCs used on rotating components within modern aero-turbines are deposited onto the Ni-base superalloy airfoils (with intervening bond coat) by electron beam methods. This method allows precise control of the thickness of the 7YSZ layer and results in a columnar microstructure, incorporating inter-columnar gaps and intra-columnar porosity. The former influences the compliance of the layer, while the latter affects its through-thickness thermal conductivity. The in-plane compliance limits the elastic energy, U_{el}, that can be stored in the layer because of its thermal expansion misfit with the substrate. Delamination of the coating is strongly affected by U_{el} through the in-plane Young's modulus, E_Π. Yet, direct measurements of this modulus are challenging and sparse. A fundamental difficulty is that removal of the coating from the substrate to make measurements causes it to fragment: its properties must be measured while still attached. Methods based on measurement of the acoustic wave velocity or of the vibration frequency can be used, but cannot be applied *in-situ* to the TBC deposited on actual airfoils. The purpose of this portion of the project was to devise and employ a suitable test protocol and to measure the in-plane modulus and tensile strength of an EB-PVD 7YSZ top coat provided by Pratt & Whitney.

Experimental method and results. The experimental protocol relies on micro-scale electro-discharge machining (EDM) to create an end-supported bilayer beam comprised of the TBC coating and a thin section of the underlying bond coat. To create this configuration a cylindrical burner bar specimen is first sliced to create a disc and then a micro-EDM is used to remove segments of the substrate while retaining the bilayer beam, as shown in Fig. 9.

To introduce bending loads into the beam a micro tensile testing setup mounted to an air table is equipped with a steel hook to pull from the inside at the center of the beam. A 5-axis piezo stage allows precise alignment of the hook relative to the beam center and the load axis. The load is measured using a 10 lb load cell. The strain is tracked by an optical camera (Pixelink, PL-782) attached to an optical microscope, which allows a change in the field of view (FOV) corresponding to magnifications ranging from 50 to 400X. In combination with the camera the FOV can be varied from 3.2 x 2.3mm down to 400 x 290µm. The displacement and strain fields are calculated from a series of images by the use of a Digital Image Correlation (DIC) technique. The DIC software suite was developed at Johns Hopkins University and utilizes Matlab (Mathworks) as the calculation engine and can be downloaded for free.
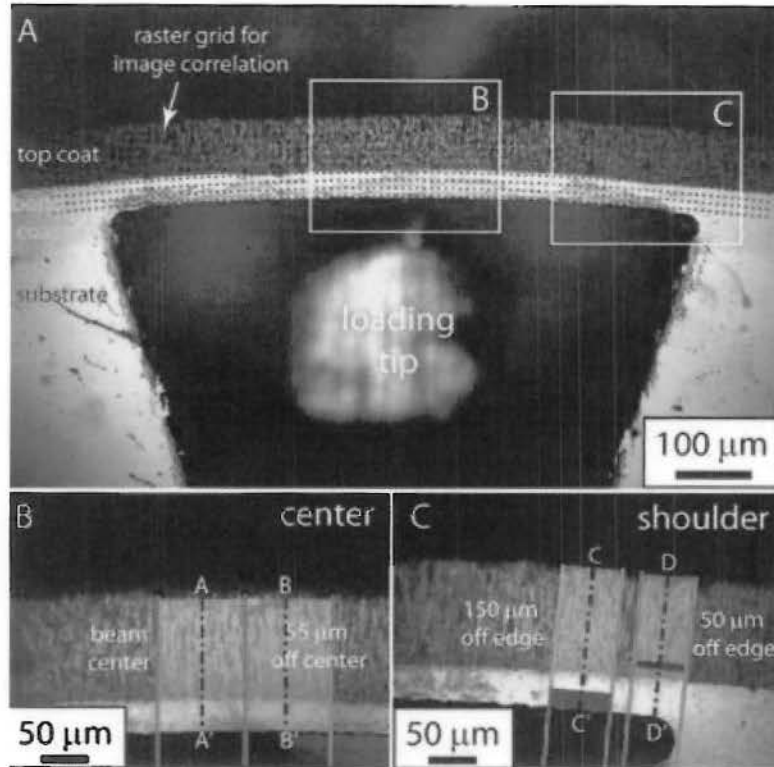
Fig. 9: (a) An optical image of the cross section of the test configuration generated from a cylindrical burner rig specimen by using micro-EDM. High-magnification optical images of the **(b)** central portion and **(c)** shoulder region of the beam. The raster grids for image-based strain measurement are superimposed on the images.

A dense displacement field with a raster size of 1 micron at 400x magnification is calculated in a post processing step. The displacement field is used to measure strains locally from the displacement gradient relative to the first image: $\varepsilon = \Delta l/l$. The DIC strain resolution is limited by image noise and vibration. To achieve a strain resolution, $d\varepsilon = 2\times10^{-4}$, the DIC raster points are averaged over a sample area of 5×50 μm^2. This allows a spatial strain resolution of 5 μm in one direction but only 50 μm in the perpendicular direction.

The axial strain (ε_{xx}) was measured as function of position from the top of the TBC for a series of increasing loads and representative curves are shown in Fig. 10. Curves taken at the center of the beam show that the axial strain varies as expected from elementary beam theory. The highest tensile strain is found at the surface of the top coat. Progressing through the top coat from the surface to the interface shows an almost linear decrease in strain. The strain crosses zero and therefore delineates the neutral plane at a depth that is near the TBC / bond coat interface. The magnitude of the strain in the top coat was measured to vary with both position along the beam and load, with a maximum strain of 3.7×10^{-3} measured at the center of the beam under a maximum load of 2.4 N.

Plots of force normalized strain verses depth (Fig. 11) show that the magnitude of the strain in the TBC scales with applied load while the neutral plane does not. The finding that the normalized strain distributions collapses to a universal curve underlines the fact that the compliance of the beam is not changing with strain as is generally hypothesized.
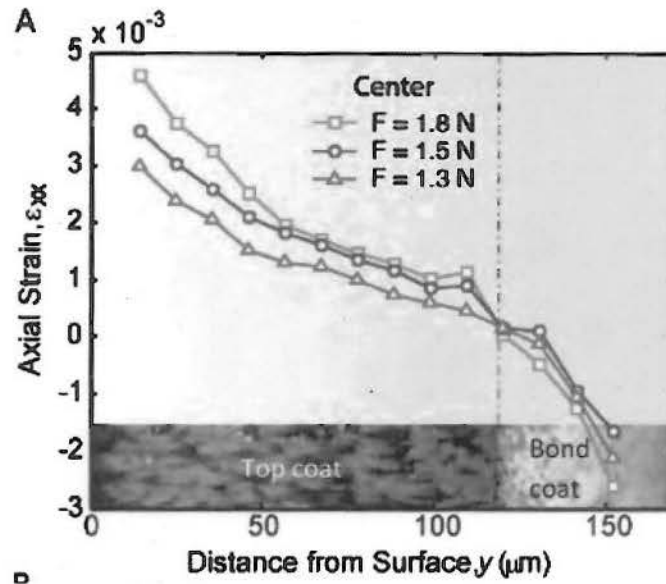
Fig. 10: Axial strain profiles obtained from the center of the beam. The in-plane strains are tensile near the surface of the TBC, go through zero near the bond coat / TBC interface, and are compressive in the bond coat.
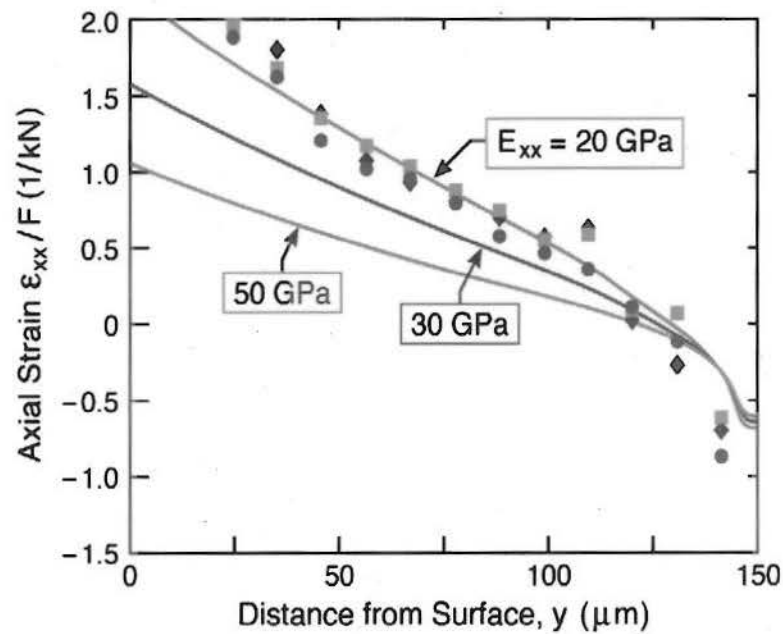

Fig. 11: Experimental measurements of axial strain profiles normalized to the applied loads that were measure in the center of the beam. The solid lines are FE predictions of based on the geometry of the samples and assumed in-plane elastic moduli. The data is best described with an in-plane modulus of 20GPa.

Analysis. The response has been analyzed by the finite element method using the commercial code ABAQUS Standard. The bond coat was considered to be elastic/plastic with power law hardening having the stress/strain curve presented earlier (yield strength, $\sigma_Y = 750 MPa$, Young's modulus, $E = 155 GPa$ and strain hardening exponent, $n = 0.2$). The TBC was assigned a strain-dependent, in-plane modulus, E_Π (1) with parameter choices in the range: $10 \leq E_0 \leq 50 GPa$ and $10^{-3} \leq \varepsilon_0 \leq 10^{-2}$. The out-of-plane modulus (which has minimal effect on the strains) was taken to be, $E_\perp \approx 160 GPa$ (compared to $E_{solid} = 200 GPa$ for dense YSZ). The results of the finite element analysis are compared with the experimental data in Fig. 11 The best fit to the experimental data was derived by using an in-plane modulus of 20GPa and no strain dependence of the modulus.

The approximate magnitude of the Young's modulus of the coating was also estimated from measurements of the location of the neutral plane. Namely. for two materials, thickness h_1 and h_2, having (strain invariant) Young's modulus, E_1 and E_2, respectively (the former being lower), subject to a bending moment (no axial force), the neutral plane is located at distance from the tensile surface, given by:

$$\frac{h_o}{h_1} = \left[1 + \frac{2E_2 h_2}{E_1 h_1} + \frac{E_2 h_2^2}{E_1 h_1^2} \right] \left[2(1 + \frac{E_2 h_2}{E_1 h_1}) \right]^{-1}$$

Note that this location depends *only on the thickness of the layers and their modulus* (not on load). Inserting the location of the neutral plane, ascertained from the ε_{xx} strains, indicates a benchmark value for the in-plane TBC modulus. , This E_0 is used as a trial, strain-invariant value for FE calculations of the strains along AA. The results for the normalized values indicate that the tensile modulus is $E_0 \approx 20 GPa$, which agrees well with the FE.

V. *In Situ* measurement of the toughness of the TGO/bond coat interface.

Difficulties associated with the measurement the interface fracture toughness of metal oxide interfaces are well documented. Variants on a notch flexure test have been most widely exploited for this purpose, particularly for interfaces in multilayer semiconductor devices. This test typically measures the mixed mode toughness, at a phase angle of 50° and is applicable to interfaces within planar devices, primarily on thin substrates. It cannot be applied to either thick or curved substrates. A new flexure test method that obviates this limitation and allows *in situ* measurement on films and coatings attached to substrates was developed for this study and used to measure the toughness between an oxide coating and a relatively small diameter cylindrical substrate.

The test design is guided by beam theory solutions for a planar configuration. In the absence of residual stress, the energy release rate, G_p, for this configuration can be expressed in the normalized form: $G_P E_2 h_2^3 / (PL)^2 \equiv \Pi(a/L, h_1/h_2, E_1/E_2, b/L)$, where P is the load/width, a is the delamination length, L is the span, b is the separation of the load points, h_1, h_2 are the thickness of the coating and substrate, respectively, and E_1, E_2 the corresponding values of

the Young's modulus. The desirable feature is that the energy release rate diminishes with increase in crack length, so that the delamination progresses *only upon increasing the load* (stable behavior). In the presence of residual stress, σ_R, another non-dimensional group influences G_P, given by: $\Re \equiv \sigma_R h_1^2 / PL$. The influence of residual stress can be substantial. Ultimately, to take into account these stresses, a finite element solution for the actual system is needed.

Measurement Protocol. In this study, specific measurements were performed on burner rig bars with columnar TBC generated by electron beam physical vapor deposition (EB-PVD) on a single crystal Ni-based superalloy substrate with a NiCoCrAlY bond coat. During deposition of the coating, a thin thermally-grown-oxide (TGO) layer develops, consisting largely of α-Al$_2$O$_3$. To create the test configuration (Fig. 9), a section of the substrate is removed by micro electro-discharge machining (EDM) to leave an intact bilayer beam along an arc of the surface. The specimen has a span to thickness, *L/h=3*, coating to substrate thickness ratio, $h_1 / h_2 = 3$, and modulus ratio, $E_2 / E_1 \approx 6$. The experiment is carried out on the custom-built micro tensile setup described in the previous section. Steel micro hooks are connected to a piezoelectric stepper motor fixed to a 5-axis stage to enable the precise alignment of the loading axis. To reduce the influence of vibrations the setup is mounted to an air table. The test is conducted in two steps. Initially, single-center-point loading is used to induce a vertical crack that extends through the coating to the interface. Thereafter, an asymmetric single point load is used to propagate the crack stably along the interface. The loads at which this happens provide a measure of the toughness.

The key experimental feature needed to analyze the measurements with high fidelity is the ability to use a digital image correlation or tracking (DICT) technique to observe *in situ* the local displacements. For this purpose, the sample deformation is monitored by a high-resolution CMOS camera (Pixelink A782) mounted to an optical microscope with a field of view ranging from 3.2 x 2.3mm to 400 x 290µm. The displacement field is calculated from a series of images captured by a digital image correlation technique. The achievable displacement resolution is limited to the vibrations, the quality of the optical system, the camera resolution and the signal to noise ratio of each pixel in the image. A dense displacement field is calculated from the acquired image sequence in a post process. This is achieved using a virtual mesh of markers with a pitch size of 1-2µm, corresponding to roughly 10-20 pixels at the highest magnification, defined and tracked by the DICT functions. The size of the tracked markers is approximately 20x20 pixels². The local displacement gradient is used to calculate the strain, $\varepsilon = \partial u / \partial x$, and the local displacement gives the opening displacement along the crack. The strain and displacement resolutions are increased by averaging the displacement gradient over a finite number of tracked markers.

Crack propagation is tracked by analyzing the displacement field using custom Matlab functions. After defining the interface in the acquired images, the crack opening displacement along the interface is measured and correlated to the applied load. To increase the sensitivity of the method, the cumulative crack opening displacement is plotted and the integrated angular change between adjacent areas of the material are used to identify the crack length.

Experimental results. A pre-crack is induced at the geometric center by single point symmetric loading. This crack follows the columnar microstructure and proceeds from the surface down to the interface. Two different methodologies have been used to extend the interface crack: designated asymmetric single-point loading (ASPL) and symmetric two-point loading (STPL). The latter is inspired by the analysis performed by Evans and Hutchinson. Tests conducted in this manner are the most straightforward to interpret. However, asymmetric loading is found to provide experimental advantages, albeit that the interpretation then requires finite element solution; the FE mesh is depicted on Fig. 12. It emerged as the method of choice.
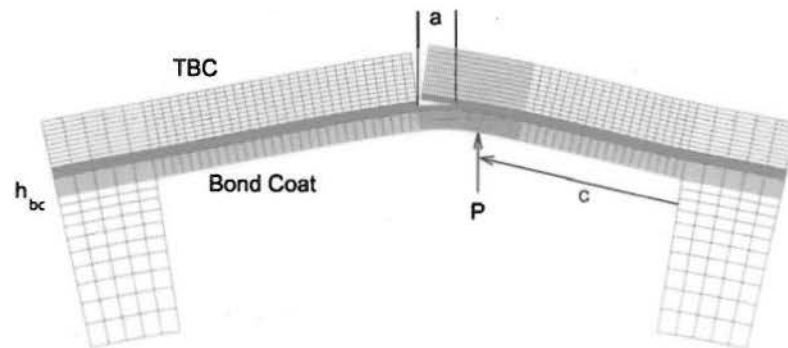

Fig. 12: The finite element mesh used to analyze the asymmetric single point loaded tests.

In this method, a dominant interface crack was generated from the pre-crack by relocating the load point off-center. This mode of loading caused an interface crack to form and propagate toward the load point in a stable manner. The ensuing interface crack path is shown in Fig. 13. It penetrates the TGO and then follows the interface with the bond coat. The tip region comprises a series of *en echelon* micro cracks traversing the TGO (Fig. 13), indicative of a mode II mechanism, as elaborated later.
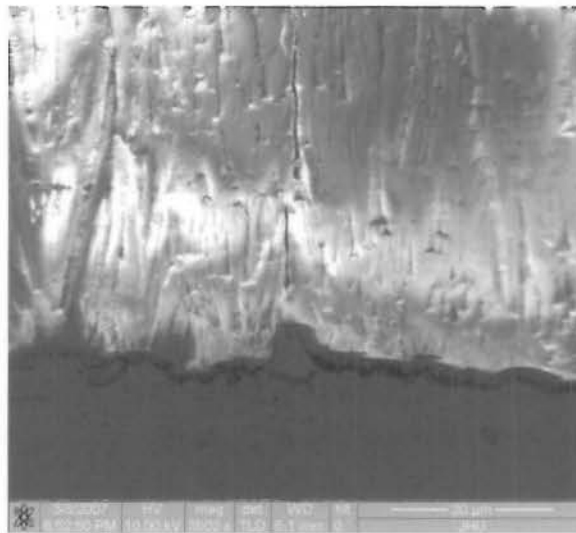

Fig. 13: A scanning electron image of the region near the center of a test specimen revealing both the vertical pre-crack and the horizontal delamination between the TGO and bond coat.

The crack tip position is revealed by displacement fields generated using the DCIT technique as illustrated in Fig. 14. Based on these profiles, the critical loads at which the delamination extends can be accurately ascertained as a function of the delamination length.

Energy Release Rates and Interface Toughness. Finite element (FE) results have been obtained for the precise system geometry, using the commercial code ABAQUS/Standard. While detailed results are presented for only one of the test sequences (experiment 5), similar features emerge in all tests. Note that the delamination is placed just within the TBC to avoid the complexities associated with a crack on a bimaterial interface. The load point is situated at distance c from the support. The following material properties and dimensions are used:

$$L = 1.1mm, \, h_{bc} = 36\mu m, \, h_{tbc} = 112\mu m,$$
$$E_{bc} = 155GPa, \, E_{tbc}^P = 20GPa, \, E_{tbc}^\perp = 180GPa, \, c = 390\mu m.$$

Based on these properties and dimensions, ABAQUS allows the energy release rate to be determined as a function of the crack length. The results are presented in the normalized coordinates suggested by beam theory, $G_p E_{bc} h_{bc}^3 / (Pc)^2$ as a function of a/L (Fig. 15). Note that, at fixed load, the energy release rate decreases as the crack extends, re-affirming the stable nature of this test configuration. The modes I and II stress intensity factors, K_I, K_{II} can also be determined from the finite element output by invoking orthotropy rescaling results. They are ascertained from the crack surface displacements at distance r from the crack front using:

$$\delta_x = 8\lambda^{-1/4} n K_{II} (r/2\pi)^{1/2} E_{tbc}^P$$
$$\delta_y = 8\lambda^{-3/4} n K_I (r/2\pi)^{1/2} E_{tbc}^P$$

$$n = [(1+\rho)/2]^{1/2}$$
with

$$\lambda = E_{tbc}^\perp / E_{tbc}^P \approx 8$$
$$\rho = [E_{tbc}^P / (2G_{12}) - \nu_{12}]\lambda^{1/2}$$

The critical values at the loads used to extend the cracks are plotted on Fig. 16(a). Based on these stress intensity factors, the mode mix can be ascertained, $\Psi = \tan^{-1}(K_{II}/K_I)$, as plotted on Fig. 15(b). Note that it is in the range $20^0 \leq \Psi \leq 40^0$.

The fracture resistance, Γ_R, can be obtained from the energy release rate (Fig. 15) by incorporating the critical loads. It can also be obtained from the stress intensity factors presented on Fig. 16(a) by using:

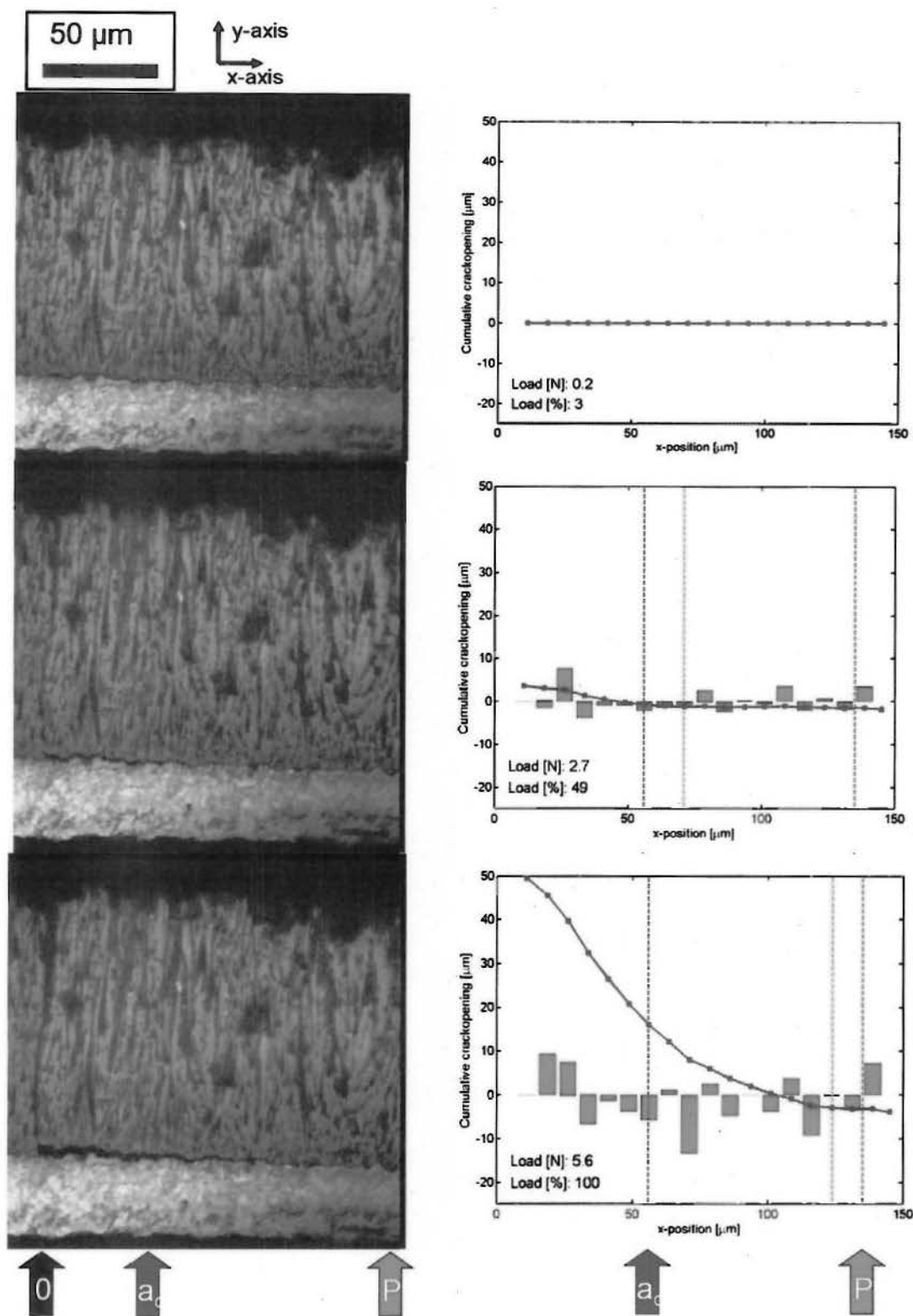$$\Gamma_R = (n/E_{tbc}^P)[\lambda^{-3/4} K_I^2 + \lambda^{-1/4} K_{II}^2]$$

Fig. 14: Experimental determination of the position of the interfacial crack tip as a function of applied load.
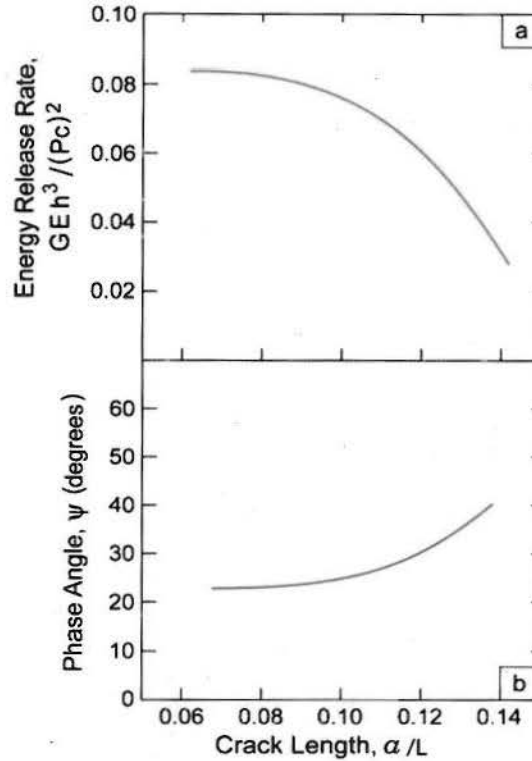
Fig. 15: (a) The non-dimensional energy release rate as a function of relative interface crack length for the asymmetric single point test with the following dimensions: span, *2L= 1.06mm*, location of load point, *c = 0.39mm*, beam width, *w= 0.51mm.* (b) Corresponding mode mix (in degrees).

The results are plotted on Fig. 17(a). It ranges from about 40 to 70Jm^{-2} for a crack extension, $\Delta a \approx 60\,\mu m$. Because the phase angle simultaneously increases from 20 to 40^0 over this interval, it is unclear whether this increase in Γ_R represents a mode mixity effect on toughness or a rising resistance with crack extension.

The caveat on the foregoing results is that any residual stress in the TBC will influence the energy release rate and mode mix and affect the interpretation. Since this stress is not known, hereafter we simply explore the likely consequences. The potential influence is estimated using the misfit stress, $\sigma_R \approx E_1 \Delta \alpha \Delta T / (1 - \nu_1)$, with $\Delta \alpha$ being the thermal expansion misfit between the coating and substrate and ΔT the temperature difference between ambient and the stress-free state for the coating. Inserting representative values indicates that, $\sigma_R \approx -100\,MPa$. The modes I and II stress intensity factors associated with this stress, ascertained using ABAQUS, are plotted on Fig. 17(b). *Note that they are both negative.* Consequently, when a load is imposed during flexure testing, initially, the net stress intensity *decreases* and becomes zero. Further elevations in the load then cause positive values to develop until the critical condition is reached. The ensuing energy release rate can be ascertained by separately adding the modes I and II stress intensities. The general features are as follows. The stress intensities at the critical loads are lower than in the absence of residual stress. Consequently, the fracture resistance inferred from the measurements is lower (Fig. 17b), ranging from 5 to 20Jm^{-2} for a crack extension, $\Delta a \approx 60\,\mu m$. Moreover the phase
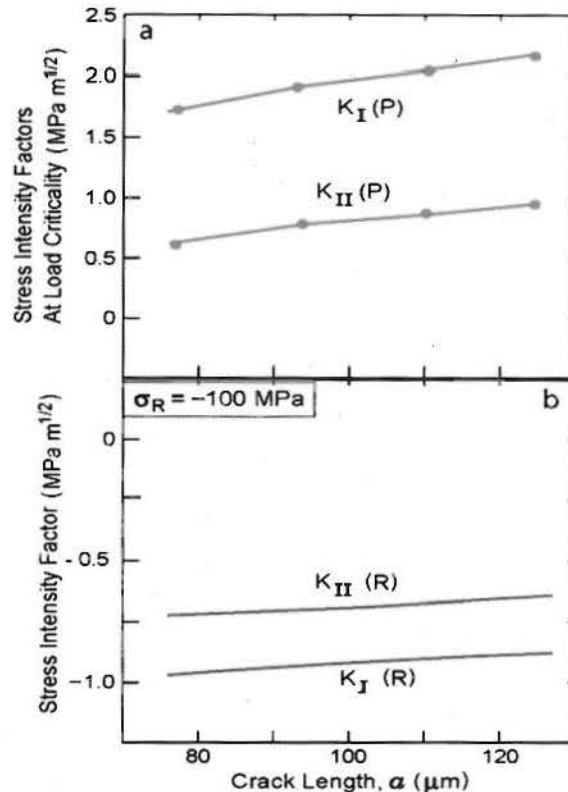
Fig. 16: The interface crack growth resistance as a function of crack extension ascertained from the ASPL test measurements. Also shown is the mode I contribution to the energy release rate at the critical load.

angle also decreases and becomes essentially mode I. When direct measurements of the residual stress become available, given the linear dependence of K on σ_R, it would be straightforward to use the stress intensities from Fig. 16 to re-compute the energy release rates and mode mixities.

Wedge indentation experiments by Evans and co-workers indicate that the energy density in the Pratt & Whitney thermal barrier system becomes supercritical beyond a critical TGO thickness. The wedge indentation experiments resulted in large scale spallation with edge sites where the TGO and top coat separated from the bond coat and substrate but did not spall. Hutchinson and Evans have derived buckling models that incorporate measured local geometry and the elastic properties of the various layers in a way that allows them to determine the fracture toughness of the TGO – bond coat interface. Preliminary results suggest a value of $\Gamma = 60\text{-}80 Jm^{-2}$ for mode II, which is in good agreement with the measurement reported here.
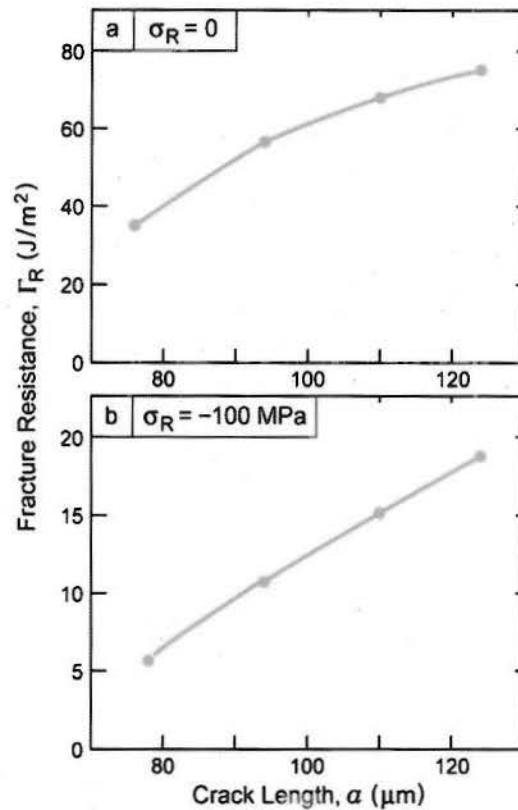
Fig. 17: Finite element calculations of the energy release rate in the presence of residual compression in the coating.

5. Incorporation of measured properties into the design code.

Wei and Hutchinson have previously developed a model for the steady-state extension of cracks along metal/oxide interfaces. That model uses an embedded process zone (EPZ) to represent the bond rupture characteristics at the crack front, allows plastic deformation to occur on either side of the interface. In the NOMELT Program, Hutchinson, through continued collaborations with Wei and Evans, developed a modified version of the Wei Hutchinson model that permits inclusion of a strain gradient plasticity length scale. The EPZ parameters used as input for this code are based on Smith's first-principles results for W_{sep} and $\hat{\sigma}$. The experimentally measured parameters that are incorporated into this model were provided by Hemker (as described in this report) and included: the elastic and plastic properties of the bond coat as well as the elastic top coat properties, as outlined in Table I.

The experimentally measured values of the interfacial toughness provided a much need benchmark for the Wei Hutchinson code. The code that was developed in this MEANS-II Program predicts trends in the toughness with stoichiometry, segregation and dopant, as a function of the yield strength of the bond coat adjacent to the interface and the characteristic

plasticity length scale due to the geometrically-necessary dislocations that accumulate in the plastic zone. We note that this type of integrated length-scale modeling has never been accomplished before for a problem that incorporates atomistics with plasticity and fracture.

Table I: Information passed to modelers in NOMELT Program

Bond coat properties and information

- Phase transformations but not dominant
- CTE of near-TGO γ layer > 25ppm°C^{-1}
- E_{bc}=155GPa, $\sigma_{y,bc}$=700MPa, N_{bc}=0.2, $l_{1,bc}$=50nm

TBC properties

- $E_{yy\ ysz}$ ~150GPa, $E_{xx\ ysz}$=20GPa

Measured interfacial properties

- Γ_{45} = 40-60 J/m2 ... Γ_1 = 30 J/m2

Calculated interfacial properties

- Γ_0 = 1 or 3 J/m^2 (clean) -or- 2 J/m^2 (with S + Hf)
- σ_{max} = 8.3 GPa

JHU Personnel Supported
- Kevin Hemker: Professor, Johns Hopkins University, Baltimore MD.
- Budhika Mendis: Post-doctoral Fellow, Johns Hopkins University, Baltimore MD.
- Chris Eberl: Post-doctoral Fellow, Johns Hopkins University, Baltimore MD.
- Xi Wang, partial support, Post-doctoral Fellow, Johns Hopkins University, Baltimore MD.
- Siriyara Suresha, partial support, Post-doctoral Fellow, Johns Hopkins University, Baltimore MD.
- Rongmei Niu, partial support, Post-doctoral Fellow, Johns Hopkins University, Baltimore MD.
- Dan Butler, partial support, Ph.D. student, Johns Hopkins University, Baltimore MD.
- John Sharon, partial support, D. student, Johns Hopkins University, Baltimore MD.

- Tim Rupert, Undergrad research assistant, Johns Hopkins University, Baltimore MD.
- Scott Hoffmann, Undergrad research assistant, Johns Hopkins University, Baltimore MD.
- Alexander Bodell, Undergrad research assistant, Johns Hopkins University, Baltimore MD.
- Peggy Hou, Visiting Scientist from LBL, Berkeley, CA.

Collaborators:
- Anthony Evans: Professor, UCSB, Santa Barbara, CA.
- Craig Steeves: Post-doctoral Fellow, UCSB, Santa Barbara, CA.
- Lorenzo Valdevit: Post-doctoral Fellow, UCSB, Santa Barbara, CA.
- John Hutchinson: Professor, Harvard University, Cambridge, MA.
- Lars Mikkelsen, Research Associate, Harvard University, Cambridge, MA.
- Tresa Pollock, Professor, University of Michigan, Ann Harbor, MI
- Brian Tryon, Post-doctoral Fellow, University of Michigan, Ann Harbor, MI
- Dan Widrevitz, Graduate Student, University of Michigan, Ann Harbor, MI
- John Smith, Dept. Head of Manuf. Processes & Systems, Delphi Research Labs, Troy, MI
- Yong Jiang, Post-doctoral Fellow, Delphi Research Labs, Troy, MI
- David Srolovitz, Professor, Princeton University, Princeton, NJ.
- Ramanathan Krishnamurthy, Post-doctoral Fellow, Princeton University, Princeton, NJ.

Publications

1. B.G. Mendis, K.J.T. Livi, and K.J. Hemker, "Observations of reactive element gettering of sulfur in thermally grown oxide pegs", *Scripta Materialia* **55** (2006) 589-592.

2. B. G. Mendis, B. Tryon, T. M. Pollock and K. J. Hemker, "Microstructural observations of as–prepared and thermal cycled NiCoCrAlY bond coats", *Surface and Coatings Technology,* **201** (2006) 3918-3925.

3. K.J. Hemker and W.N. Sharpe, Jr., "Microscale Characterization of Mechanical Properties", *Annu. Rev. Mater. Res., 37 (2007) 93–126.*

4. BG Mendis, KJ Hemker, Evolution of the premartensitic state in the NiAl phase of a NiCoCrAlY bond coat during thermal cycling, *Philosophical Magazine,* **87** (2007) 4229-4251.

5. BG Mendis, KJ Hemker, Thermal stability of microstructural phases in commercial NiCoCrAlY bond coats. *Scripta Materialia,* **58** (2008) 255-258.

6. K.J. Hemker, B. G. Mendis and C. Eberl, "Characterizing the microstructure and mechanical behavior of a two-phase NiCoCrAlY bond coat for thermal barrier systems", *Materials Science and Engineering A,* 483–484 (2008) 727–730.

7. C. Eberl, D.S. Gianola, K.J. Hemker, "Mechanical characterization of coatings with microbeam bending and digital image correlation techniques", *Experimental Mechanics,* (2008) in press.

8. C. Eberl, D.S. Gianola, M.Y He, A.G. Evans, K.J. Hemker, "A Method for In Situ Measurement of the Strain Dependence of the Elastic Properties of a Columnar Thermal Barrier Coating", in preparation.

9. C. Eberl, D. S. Gianola, K.J. Hemker, M. Y. He, A. G. Evans, "In Situ Measurement of the Toughness of the Interface Between a Thermally Grown Alumina and a Ni Alloy", in preparation.

Transitions
- Nothing specific at JHU.

Awards Received
- Professor Hemker named a Fellow of ASME in December 2007.